

Hybrid Electrochemical/Chemical Synthesis of Supported, Luminescent Semiconductor Nanocrystallites with Size Selectivity: Copper(I) Iodide

G. S. Hsiao,[†] M. G. Anderson,[†] S. Gorer,[†] D. Harris,[‡] and R. M. Penner^{*,†}

Contribution from the Department of Chemistry, Institute for Surface and Interface Science, University of California, Irvine, California 92697-2025, and Charles Evans and Associates, 301 Chesapeake Drive, Redwood City, California 94063

Received September 3, 1996[⊗]

Abstract: β -CuI nanocrystallites (NCs) are synthesized on the atomically smooth graphite basal plane surface using a new hybrid electrochemical/chemical (E/C) method. This method involves the following steps: (1) electrochemical deposition of copper NCs onto an electrode surface, (2) electrochemical oxidation of these copper NCs to yield Cu₂O, and (3) displacement of oxygen in Cu₂O by iodide in an aqueous KI solution. Dispersions of CuI NCs having mean diameters ranging from 10 to 180 Å were prepared using the E/C method. Selected-area electron diffraction analysis reveals that β -CuI NCs are obtained; these NCs are epitaxially aligned with the hexagonal periodicity of the graphite surface, as are the Cu₂O precursor particles. For samples of supported CuI NCs having a mean particle height of <25 Å, individual NCs were well-separated from one another on the graphite surface and were narrowly dispersed in height. Photoluminescence spectroscopic analysis showed a strong, room temperature emission at an energy corresponding to the band gap. As the crystallite diameter was reduced from 180 Å to 13 Å, the energy of this emission shifted from the macroscopic value of 2.92 eV to >3.04 eV, in good agreement with the predictions of the effective mass, strong confinement model.

I. Introduction

In recent years, the size-dependent physical properties exhibited by semiconductor nanocrystallites (NCs) have been extensively studied.^{1–3} To date, most experimental data pertaining to the electronic properties of semiconductor NCs has been obtained via spectroscopic investigations of *suspensions* of NCs in a variety of media. But while suspensions of semiconductor NCs are convenient for optical investigations, future technological applications are likely to require the immobilization of NCs on the surfaces of conductors or semiconductors. Previously, this immobilization has been accomplished using either of two general strategies: The first is the transferral of semiconductor NCs from a suspension to a surface; the second involves the direct synthesis of semiconductor NCs on a surface of interest.

Previously, the direct synthesis of semiconductor nanocrystals on surfaces has been accomplished using both molecular beam epitaxy (MBE) and chemical vapor deposition (CVD) based methods. Examples include the MBE “self-organized” growth of InAs islands on GaAs⁴ and InP islands on GaInP⁵ and the Stranski-Krastanov CVD growth of SiGe islands on Si.^{6,7} However in general, the average diameter of NCs synthesized

by MBE and CVD cannot readily be adjusted because it depends on factors intrinsic to the interface which is obtained upon deposition such as the lattice mismatch between the deposited material and the substrate. The epitaxial electrodeposition of semiconductor nanocrystallites has recently been accomplished for the first time by Hodes, Rubinstein, and co-workers.^{9–11} These workers have epitaxially grown high-quality, wurtzite CdSe nanocrystallites on Au(111) surfaces by galvanostatic deposition. Like MBE-based syntheses, it has been demonstrated that the interfacial strain energy determines the nanocrystallite diameter,¹² and for CdSe nanocrystals deposited using this method, a quantum confinement based increase of the band gap has been observed for particles with a diameter $d < 50$ Å using an atomic force microscope (AFM) based current–voltage spectroscopy.¹³

In this paper, a new hybrid electrochemical/chemical (henceforth E/C) method for preparing supported semiconductor nanocrystallites is described. The E/C method involves three discrete steps, as shown schematically in Figure 1 for β -CuI, the material of interest in this paper: (1) electrochemical deposition of copper nanocrystallites on the surface of an electrode, (2) electrochemical oxidation of copper nanocrystallites to cubic Cu₂O, and (3) displacement of the oxygen in the Cu₂O by iodide in an aqueous potassium iodide solution to obtain semiconducting β -CuI nanocrystallites. In contrast to the surface synthesis methods described above, the CuI NCs

* Address correspondence to this author at rmpenner@uci.edu.

[†] University of California.

[‡] Charles Evans and Associates.

[⊗] Abstract published in *Advance ACS Abstracts*, January 1, 1997.

(1) Bawendi, M. G.; Steigerwald, M. L.; Brus, L. E. *Annu. Rev. Phys. Chem.* **1990**, *41*, 477.

(2) Henglein, A. *Chem. Rev.* **1989**, *89*, 1861.

(3) Steigerwald, M. L.; Brus, L. E. *Acc. Chem. Res.* **1990**, *23*, 183.

(4) Marzin, J.-Y.; Gerard, J.-M.; Izrael, A.; Barrier, D.; Bastard, G. *Phys. Rev. Lett.* **1994**, *73*, 716.

(5) Castrillo, P.; Hessman, D.; Pistol, M.-E.; Anand, S.; Carlsson, N.; Seifert, W.; Samuelson, L. *Appl. Phys. Lett.* **1995**, *67*, 1905.

(6) Apetz, R.; Vescan, L.; Hartmann, A.; Dieker, C.; Luth, H. *Appl. Phys. Lett.* **1995**, *66*, 445.

(7) Schittenhelm, P.; Gail, M.; Brunner, J.; Nutzel, J. F.; Abstreiter, G. *Appl. Phys. Lett.* **1995**, *67*, 1291.

(8) Reference deleted in revision.

(9) Golan, Y.; Margulis, L.; Rubinstein, I.; Hodes, G. *Langmuir* **1992**, *8*, 749.

(10) Golan, Y.; Margulis, L.; Hodes, G.; Rubinstein, I.; Hutchinson, J. L. *Surf. Sci.* **1994**, *311*, L633.

(11) Golan, Y.; Ter-Ovanesyan, E.; Manassen, Y.; Margulis, L.; Hodes, G.; Rubinstein, I.; Bithell, E. G.; Hutchinson, J. L. *Surf. Sci.* **1996**, *350*, 277.

(12) Golan, Y.; Hodes, G.; Rubinstein, I. *J. Phys. Chem.* **1996**, *100*, 2220.

(13) Alpers, B.; Cohen, S.; Rubinstein, I.; Hodes, G. *Phys. Rev. B* **1995**, *52*, 17017.

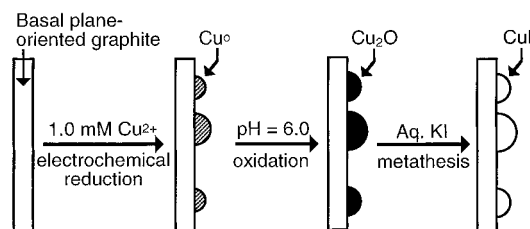


Figure 1. Schematic diagram of the hybrid electrochemical/chemical (E/C) method employed for the synthesis of CuI in this paper.

obtained by the E/C method on graphite are immobilized via relatively weak van der Waals forces; however, an epitaxial alignment of these nanocrystals with the hexagonal periodicity of the graphite surface is never the less obtained. A characteristic feature of the E/C synthetic method is that the size and size monodispersity of the semiconductor nanocrystals which are obtained are decided by the corresponding characteristics of the metal nanocrystallites which are deposited electrochemically in step 1 above. At graphite surfaces, the deposition of metal NCs at high overpotentials occurs via an instantaneous nucleation and growth mechanism which yields a relatively narrow particle size distribution. In addition, because both steps 1 and 2 are, in principle, applicable to a variety of different metals, a variety of I–VII and II–VI compound semiconductors may be accessible using variants of this approach.

We have chosen to study CuI here because the copper NCs required for step 1 of the E/C synthesis are readily obtained from dilute, aqueous Cu^{2+} solutions at graphite electrode surfaces using a pulsed potentiostatic deposition method as previously described.^{14,15} As we shall see, the E/C synthesis of CuI yields β -CuI which has a wurtzite crystal structure and a direct band gap at 3.06 eV.¹⁶ CuI has a small Bohr exciton radius of 15 Å,¹⁷ and CuI NCs are considered excellent candidates for the investigation of the weak (or exciton) quantum confinement size effect.^{18,19} However, the quantum size effect for CuI is controversial: Itoh et al.²⁰ (working with NCs of unreported size polydispersity) and Gogolin et al.²¹ have classified as weak the quantum size effect in CuI, whereas Masumoto et al.¹⁷ have reported absorption data consistent with the strong confinement model. In fact, the theoretical treatment of Kayanuma¹⁹ predicts that, for CuI NCs smaller than 60 Å, the quantum size effect should be strong. All previous work with CuI nanocrystals has involved suspensions in silica glass or salt matrices, and quantitative work with this material has been impeded by the absence of methods (either liquid solution or surface-based) for preparing CuI NCs which are narrowly dispersed in size, and for which the critical particle parameters (crystallinity, crystal structure, and monodispersity) are directly measurable. The supported CuI NCs obtained using the E/C method therefore meet an important need. We shall show that the fluorescence properties of β -CuI NCs in the size range 13–25 Å agree quantitatively with the effective mass based strong confinement theory.

(14) Zoval, J. V.; Stiger, R. M.; Biernacki, P. R.; Penner, R. M. *J. Phys. Chem.* **1996**, *100*, 837.

(15) Zoval, J. V.; Biernacki, P.; Penner, R. M. *Anal. Chem.* **1996**, *68*, 1585.

(16) Cardona, M. *Phys. Rev.* **1963**, *129*, 69.

(17) Masumoto, Y.; Kawabata, K.; Kawazoe, T. *Phys. Rev. B* **1995**, *52*, 7834.

(18) Brus, L. E. *J. Chem. Phys.* **1984**, *80*, 4403.

(19) Kayanuma, Y. *Phys. Rev. B* **1988**, *38*, 9797.

(20) Itoh, T.; Iwabuchi, Y.; Kirihiro, T. *Phys. Status. Solidi. B* **1988**, *146*, 531.

(21) Gogolin, O.; Berosashvili, Y.; Mshvelidze, G.; Tsitsishvili, O. S.; Giessen, H.; Uhrig, A.; Klingshirn, C. *Semicond. Sci. Technol.* **1991**, *6*, 401.

II. Experimental Methods

II.A. Copper Iodide Nanocrystallite Synthesis. The following procedure was employed for CuI synthesis.

1. A freshly cleaved, basal plane oriented graphite surface was immersed in the degassed, copper plating solution, potentiostated at +100 mV (vs $\text{Cu}^{2+}/\text{Cu}^0$) for 60 s, and the potential was then stepped to -500 mV (vs $\text{Cu}^{2+}/\text{Cu}^0$) for a duration varying from 180 ms to 2 s (depending on the quantity of copper it was desired to deposit). The integrated charge was corrected for background by subtraction of the charge observed for the same surface (i.e., the same cleave) in the copper-free electrolyte described above. This corrected deposition charge varied from 40 to 480 $\mu\text{C cm}^{-2}$.

2. At the completion of the copper deposition pulse, copper NCs were electrochemically oxidized to Cu_2O at 0.0 V (vs $\text{Cu}^{2+}/\text{Cu}^0$) for 5 s.

3. The graphite working electrode was emersed from the plating solution, and residual solution was removed from the graphite surface mechanically (by vigorous shaking) followed by blow drying in a purified N_2 stream and, in some cases, by rinsing with Nanopure water ($\rho > 18 \text{ M}\Omega\text{-cm}$).

4. The oxygen displacement reaction was carried out by immersing Cu_2O NCs in an aqueous, 10 mM KI solution for 1.0 min, followed by thorough rinsing of the surface in a stream of Nanopure water.

II.B. X-ray Photoelectron Spectroscopy. X-ray photoemission spectroscopy (XPS) measurements were performed using an Al k_{α} photoline.

II.C. Transmission Electron Microscopy (TEM) and Selected-Area Electron Diffraction (SAED). TEM and SAED data were acquired on Cu_2O and CuI nanocrystallites without removal of these nanoparticles from the graphite basal plane surface. This was accomplished by preparing an HOPG working electrode consisting of a thin (100–400 Å thick) HOPG flake ($\approx 1 \text{ mm}^2$) supported on a carbon-coated copper grid. The E/C deposition of CuI was then performed on this electrode using the same procedure as described above. The copper coverage could not be determined in these experiments because copper deposition occurred both on the TEM grid and on the carbon flake. TEM data were obtained using an accelerating voltage of 200 keV, and diffraction patterns were obtained at a camera length of 1000 mm using a selected-area aperture of 10 μm diameter.

II.D. Noncontact Scanning Force Microscopy (NC-AFM). NC-AFM images were obtained using a commercial multimode scanning probe microscope in the laboratory air ambient and represent a random sampling of four or more macroscopic sites of the sample surface. Height measurements were made by comparing the height of the structures with the immediate HOPG background. Image sizes ranged from 1 to 5 μm square, and statistics were obtained from 1 μm square images acquired at 256 lines.

II.E. Fluorescence Microprobe Measurements. Fluorescence microprobe emission spectra were acquired as follows: Excitation from an argon ion laser operating at 351 nm and focused to a beam diameter of 0.2 mm was incident on the graphite surface at an angle of 60° from surface normal (external to the collection optics) in the laboratory air ambient. Fluorescence from the surface was collected at normal incidence using a 100 \times objective (N.A. = 0.75). Rayleigh scatter was eliminated from this signal using an interference filter, and the fluorescence image of the surface was spatially filtered to yield a $\approx 30 \mu\text{m}$ spot size. The signal from this area was coupled with an f4 lens into an f4 imaging spectrograph which dispersed the light onto a liquid nitrogen-cooled CCD. In conjunction with the linear dispersion produced by the 300 groove mm^{-1} grating, the pixelwise resolution of this detector was 1.4–1.9 meV depending on wavelength. Collection times ranging from 0.1 to 30 s were employed for laser powers of $\approx 30 \text{ mW}$.

III. Results and Discussion

III.A. An E/C Synthesis Strategy for CuI. In the Pourbaix diagram²² for 1.0 mM Cu^{2+} of Figure 2A, it is evident that Cu_2O is the immediate product of the oxidation of copper metal in solutions having a pH more basic than 5.3. Consistent with

(22) Pourbaix, M. *Atlas of Electrochemical Equilibria in Aqueous Solutions*; Pergamon Press: New York, 1966.

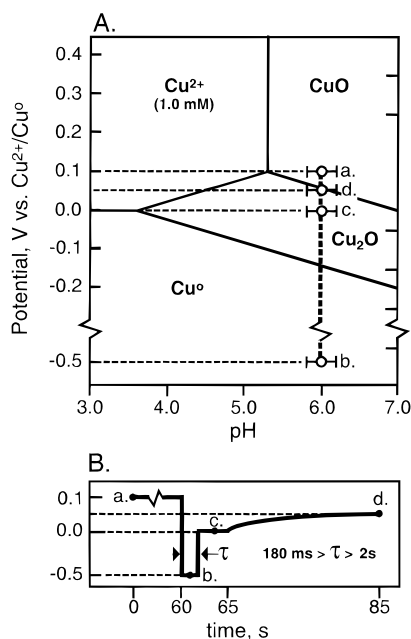


Figure 2. (A) Pourbaix diagram for copper appropriate for $[\text{Cu}^{2+}] = 1.0 \text{ mM}$ (after ref 22). Data points, labeled with lower-case letters, indicate the following junctures during the E/C synthesis of CuI: (a) initial potential, $E_{\text{appl}} = +100 \text{ mV}$ vs $\text{Cu}^{2+}/\text{Cu}^0$, applied immediately prior to copper plating pulse; (b) plating potential, $E_{\text{appl}} = -500 \text{ mV}$ applied for a duration, τ , of between 0.18 and 2 s; (c) oxidation potential, $E_{\text{appl}} = 0 \text{ mV}$; and (d) final open circuit electrode potential, $E_{\text{oc}} \approx +50 \text{ mV}$, following the stabilization of the potential at open circuit for 20 s. Horizontal error bars indicate the pH range encountered for the unbuffered copper plating solutions employed for this study. (B) Timing diagram for the electrochemical preparation of copper oxide from a 1.0 mM copper solution. The letters here indicate the same junctures as in panel A.

this prediction, it has been reported that Cu_2O is obtained via the electrochemical oxidation of copper in a variety of basic electrolytes.^{23,24} On the basis of these considerations, the following E/C procedure was employed for the synthesis of CuI nanocrystallites: First, Cu^0 nanocrystallites were deposited on the freshly cleaved graphite surface by pulsed potentiostatic deposition from a 1.0 mM Cu^{2+} solution at -500 mV (vs $\text{Cu}^{2+}/\text{Cu}^0$) and $\text{pH} = 6.0 \pm 0.2$ (Figure 2A.b). This operation would appear from the Pourbaix diagram to be impossible because of the thermodynamic instability of Cu^{2+} at $\text{pH} = 6$; however, it is readily verified that the formation of CuO from Cu^{2+} is kinetically too slow to cause any perceptible instability of this plating solution. Following the electroplating of copper nanocrystallites, these particles were electrochemically oxidized to Cu_2O in the plating solution, at 0.0 V (Figure 2A.c). The oxidation of copper NCs at the electrode surface was verified by monitoring the open-circuit potential of the graphite surface after oxidation: within 20 s of the oxidation step, the surface potential arrived at a point within $\pm 10 \text{ mV}$ of $+50 \text{ mV}$ corresponding to the intersection between the Cu_2O and CuO regions shown in Figure 2A (Figure 2A.d). Finally, Cu_2O was immersed in the KI solution in which the displacement of oxygen by iodide yielded $\beta\text{-CuI}$ in approximately 1 min.

The production of CuI from Cu_2O by displacement has literature precedents: CuI has been reported to form spontaneously at lightly oxidized copper surfaces in contact with basic iodide-containing electrolytes.²⁵ In addition, displacement has

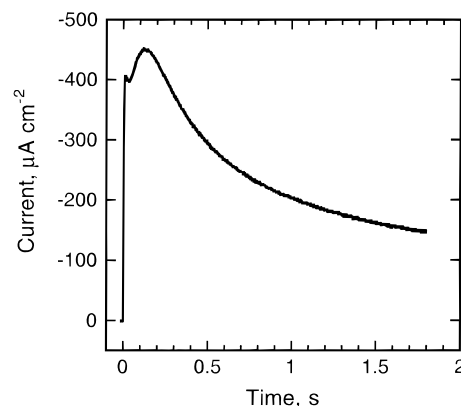


Figure 3. Cathodic current at a freshly cleaved HOPG electrode, 0.494 cm^2 in area, as copper is potentiostatically deposited at an applied potential of -500 mV vs $\text{Cu}^{2+}/\text{Cu}^0$. The deposition solution was aqueous 1.0 mM $\text{Cu}(\text{NO}_3)_2$, 10 mM K_2SO_4 . Background correction of this transient was accomplished by subtracting the current for the same electrode in a “blank” solution of aqueous 2.0 mM KNO_3 , 10 mM K_2SO_4 .

previously been employed as a means of obtaining CuI from Cu_2S at macroscopic copper surfaces²⁶ and has probably been involved in the formation of thin layers of CuI on copper surfaces in basic iodide-containing electrolytes, but this mechanism was not invoked.²⁷ The electrodeposition of copper and the characterization of the CuI nanocrystals obtained from the E/C synthesis are discussed in greater detail in forthcoming sections.

With regard to the generality of the E/C method for the preparation of other semiconducting materials, an exactly analogous E/C synthetic scheme can, in principle, be employed to synthesize $\text{Cu}^{\text{I}}\text{Cl}$ and $\text{Cu}^{\text{I}}\text{Br}$ as well as most II–VI materials such as the cadmium salts: CdS , CdSe , and CdTe . In the case of the cadmium salts, however, because no pH exists at which the metal ion plating solution (i.e., 1.0 mM Cd^{2+}) and $\text{Cd}(\text{OH})_2$ are simultaneously stable (and in contrast to the copper case, the formation of $\text{Cd}(\text{OH})_2$ at high pH occurs rapidly²²), a modification to the E/C procedure for CuI is necessary: Following the deposition of metal nanocrystallites at a pH where Cd^{2+} solution is stable (e.g., $\text{pH} = 6$), the pH must be shifted higher (e.g., to $\text{pH} = 9.0\text{--}10.0$) prior to the electrochemical oxidation of the metal to $\text{Cd}(\text{OH})_2$. $\text{Cd}(\text{OH})_2$ has previously been identified by Gorer and Hodes²⁸ as a key intermediate in the chemical solution deposition of CdSe films under most experimental conditions.

III.B. Copper Nanocrystallite Deposition and Oxidation.

Copper nanocrystallites were deposited using the pulsed potentiostatic method described earlier.^{14,15} The narrowest particle size distributions for copper particles were achieved using a large deposition overpotential of -500 mV (vs $\text{Cu}^{2+}/\text{Cu}^0$). A typical current–time transient obtained for copper deposition is shown in Figure 3. This transient is qualitatively similar to those which we have observed previously for the potentiostatic deposition of silver on HOPG at this same overvoltage:¹⁴ Promptly upon the application of the deposition pulse, an increasing cathodic current which is nearly proportional to $t^{1/2}$ is seen. This functional form for the current–time transient is produced^{29,30} by the growth of a fixed number of copper nuclei

(26) Chaudhuri, T. K.; Basu, P. K.; Patra, A. B.; Saraswat, R. S.; Acharya, H. N. *Jpn. J. Appl. Phys.* **1990**, *29*, L352.

(27) Tennakone, K.; Punchihewa, S.; Kiridena, W. C. B.; Ketiparachchi, U. S.; Senadeera, S. *Thin Solid Films* **1992**, *217*, 129.

(28) Gorer, S.; Hodes, G. *J. Phys. Chem.* **1994**, *98*, 5338.

(29) Harrison, J. A.; Thirsk, H. R. *The Fundamentals of Metal Deposition*; Harrison, J. A., Thirsk, H. R., Eds.; Marcel Dekker: New York, 1971; Vol. 5.

(23) Elsner, C. I.; Salvarezza, R. C.; Arvia, A. J. *Electrochim. Acta* **1988**, *33*, 1735.

(24) Nagy, G.; Roy, D. *Langmuir* **1993**, *9*, 1868.

(25) Irish, D. E.; Stolberg, L.; Shoesmith, D. W. *Surf. Sci.* **1985**, *158*, 238.

each by a hemispherical diffusive flux, and the important implication is that the nucleation of copper particles in these experiments is nearly temporally discrete, coinciding with the onset of the deposition voltage pulse. As the electrolysis continues, the hemispherical diffusion layers of adjacent copper nuclei merge to generate an approximately planar diffusion field, causing a peak in the current–time transient (at an integrated charge of 50–80 $\mu\text{C cm}^{-2}$), and a transition at longer times to a decaying, Cottrellian current which is proportional to $t^{-1/2}$ is seen.

The characterization of copper NCs by NC-AFM was not attempted because XPS measurements indicated that these particles oxidized rapidly upon exposure to air. Instead, immediately following deposition, copper NCs were electrochemically oxidized as indicated in the timing diagram of Figure 2B to obtain Cu_2O NCs. Cu_2O NCs were air-stable (with respect to further oxidation to CuO), and NC-AFM images of these surfaces appeared indistinguishable from images of the CuI NCs shown in Figures 6–8 (see discussion of these data below). For copper coulometric loadings in the range 40 $\mu\text{C cm}^{-2} < Q_{\text{Cu}} < 100 \mu\text{C cm}^{-2}$, corresponding to 0.07–0.18 equiv copper monolayers (assuming an adsorption electrovalency of 2.0), discrete Cu_2O particles having a mean height of 25 Å or less were observed and these particles were evenly dispersed across the atomically smooth graphite basal plane surface, as well as at defect sites such as step edges on the surface. The NC-AFM images of CuI NCs, Figure 6, provide an excellent representation of the topography seen for Cu_2O NCs in this coverage regime. Although fluctuations in the nucleation areal density were observed from experiment to experiment, as compared to our previous findings for silver nanocrystallite growth on graphite,¹⁴ the areal density of Cu_2O nanocrystallites was higher by a factor of 5 (10^{10} cm^{-2} for copper vs $5 \times 10^9 \text{ cm}^{-2}$ for silver). The particle morphology seen for Cu_2O implies that copper electrodeposition occurs via a Volmer–Weber growth mode in which three-dimensional growth occurs promptly following the formation of critical nuclei on the graphite surface, exactly as reported for silver deposition on graphite previously.¹⁴ At higher initial copper coverages, the morphology of the Cu_2O deposit became rapidly more disordered, also as qualitatively seen in the NC-AFM images of Figures 7 and 8 for CuI . A discussion of these data is deferred until later.

III.C. Conversion to β -CuI and Characterization. After the exposure of Cu_2O NCs to aqueous KI solution, the resulting CuI NCs were characterized by X-ray photoelectron spectroscopy (XPS), NC-AFM, scanning Auger microprobe (SAM) analysis, and laser-induced fluorescence measurements. We do not describe the results of SAM analyses below because the information obtained was redundant with the more detailed structural information obtained using SAED in conjunction with TEM. The results for each of the remaining techniques are summarized below.

III.C.1. Transmission Electron Microscopy/Selected-Area Electron Diffraction. The TEM image of Figure 4a was acquired immediately following the deposition of copper NCs and the electrochemical oxidation of these particles. Following TEM imaging and diffraction analysis of this surface, this sample was removed from the TEM, the surface was exposed to aqueous KI, rinsed with water, dried, and returned to the vacuum environment of the microscope, and the TEM image of Figure 4d was acquired. A careful comparison of the two TEM images, guided by the distinctive patterns of NCs which are marked with the lower-case letters u, v, and w, reveals that

the positions of NCs and the NC diameter are both preserved during the conversion from Cu_2O to CuI .

SAED patterns of this region, shown in panels b and e, allow the crystal structure and the crystallographic orientation of the NCs on the hexagonal graphite surface to be determined. Diffraction from the graphite substrate surface and NCs is simultaneously observed, and the graphite pattern therefore serves as a convenient internal calibration standard for the assignment of the NC reciprocal lattice. The diffraction spots in panel b are assigned to cubic Cu_2O whereas NC diffraction in the pattern of panel e is assigned to wurtzite β - CuI . Because the aperture employed for selected-area diffraction had a 10 μm diameter, the patterns shown in panels b and e are derived from approximately 200 NCs on the graphite surface. Thus, the single-crystal diffraction which is obtained from this ensemble of NCs is evidence that NCs of both materials are epitaxially aligned with the hexagonal periodicity of the graphite surface.

In the case of CuI , the orientation of NCs on the graphite surface may be deduced from the electron diffraction pattern as follows: Diffractions corresponding to periodicities existing along the c -axis of the unit cell (e.g. [001] and [002]) are missing whereas the strongest diffraction spot (i.e., [010]) corresponds to a 3.71 Å periodicity existing within hexagonal copper or iodide layers in the wurtzite structure. Together, these two observations indicate that the c -axis of CuI nanocrystals is oriented perpendicularly to the plane of the graphite surface and that hexagonal planes of either copper or iodide atoms, with a lattice constant of $a = 4.27 \text{ \AA}$, are in contact with the graphite surface. With this orientation, $2 \times d_{100} (= 2 \times 2.1386 \text{ \AA} = 4.2772 \text{ \AA})$ for graphite provides a near perfect match to a for CuI (mismatch = 0.02%). As shown in the schematic diagram of Figure 4g, the resulting arrangement of copper (or iodide) atoms on the graphite surface corresponds to a $(\sqrt{3} \times \sqrt{3})R30^\circ$ alignment of the two-dimensional unit cell in the (0001) planes of the CuI crystallite with the 2.47 Å hexagonal periodicity of the graphite substrate.

Taken together, the TEM and the SAED data clearly indicate that Cu_2O NCs are converted on a particle-by-particle basis to β - CuI . That is, the number of copper atoms is conserved in the conversion of a Cu_2O NC to a CuI NC. In addition, a comparison of the two TEM images (Figure 4, panels a and d) reveals that most of the particles do not move on the graphite surface during the conversion process. These observations provide justification for the schematic diagram of Figure 1 in which these two characteristics are implicit. If it can be assumed that Cu_2O NCs are obtained in a likewise fashion from the Cu^0 NCs which are initially electrochemically deposited, it is reasonable to conclude that the CuI NC diameter is decided by the diameter of the copper NCs deposited in step 1 of the synthesis. An important corollary is that improvements to the monodispersity of CuI NCs can be expected to follow improvements in the monodispersity of Cu^0 NCs which are initially deposited.

The electron diffraction data presented here constitutes the first determination of the crystal structure for CuI NCs.^{17,20,21} CuI is polymorphic, and the γ form, having a zinc blende structure, is the most stable structure at room temperature while β - CuI is obtained from γ - CuI at a temperature of 370.5 °C.¹⁶ AgI exhibits exactly analogous phase behavior, but a somewhat lower phase transition temperature.¹⁶ In previous work,^{31,32} solution-synthesized AgI NCs have been found to be β -form, so the observation of β -form CuI NCs in this work is not

(31) Micic, O. I.; Meglic, M.; Lawless, D.; Sharma, D. K.; Serpone, N. *Langmuir* **1990**, *6*, 487.

(32) Schmidt, K. H.; Patel, R.; Meisel, D. *J. Am. Chem. Soc.* **1988**, *110*, 4882.

(30) Gunawardena, G.; Hills, G.; Montenegro, I.; Scharifker, B. J. *Electroanal. Chem.* **1982**, *138*, 225.

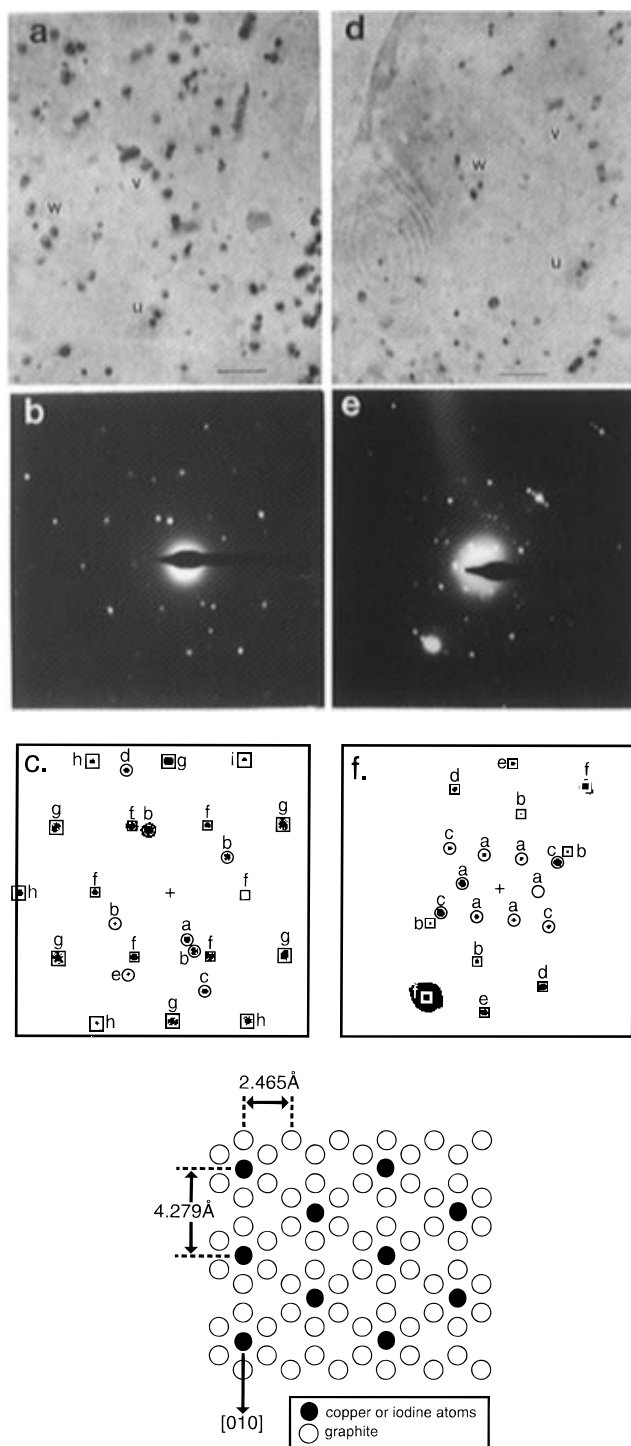


Figure 4. (a) Transmission electron micrograph (TEM) of an electron-transparent graphite surface immediately following the electrochemical deposition of copper, and subsequent oxidation. Lower-case letters (e.g., u, v, w) indicate distinctive clusters of nanocrystallites. The distance bar shown corresponds to 80 nm. (b) Electron diffraction (ED) analyses of a 10 μm diameter region centered about the TEM image of panel a. (c) Map showing assignments for the ED pattern of panel b (based on International Centre for Diffraction Data File #05-0667). Circles, labeled with the lower-case letters a–e, are assigned to cubic Cu_2O as follows: a: [110], $d = 3.02 \text{ \AA}$; b: [111], $d = 2.465 \text{ \AA}$; c: [220], $d = 1.510 \text{ \AA}$; d: [222], $d = 1.223 \text{ \AA}$; e: [211], $d = 1.743 \text{ \AA}$. Squares, labeled with the letters f–h, are assigned to graphite as follows: f: [100], $d = 2.319 \text{ \AA}$; g: [110], $d = 1.234 \text{ \AA}$; h: [112], $d = 1.16 \text{ \AA}$. (d) TEM images of the same region shown in panel a but following the immersion of the surface in aqueous 10 mM KI solution for 1 min. The distance bar shown is 80 nm, and the lower-case letters indicate the same clusters of NCs marked in panel a. (e) Electron diffraction (ED) analyses of a 10 μm diameter region centered about the TEM image of panel d. (f) Map showing assignments for the ED pattern of a panel e (based on File #45-1316). Circles, labeled with the lower-case letters a–d, are assigned to (wurtzite) $\beta\text{-CuI}$ as follows: a: [010], $d = 3.71 \text{ \AA}$; b: [020], $d = 1.85 \text{ \AA}$. Squares, labeled with the letters c–f, are assigned to graphite as follows: c: [100], $d = 2.139 \text{ \AA}$; d: [110], $d = 1.234 \text{ \AA}$; e: [112], $d = 1.16 \text{ \AA}$; f: [201], $d = 1.057 \text{ \AA}$. (g) Schematic diagram showing the orientation of $\beta\text{-CuI}$ crystallite on the graphite basal plane based on electron diffraction analysis. Hexagonal (0001) planes of copper (or iodide atoms) possesses a $(\sqrt{3} \times \sqrt{3})R30^\circ$ orientation with respect to the hexagonal periodicity of the graphite surface.

surprising. However, epitaxial alignment of the CuI NCs with the hexagonal periodicity of the graphite surface may provide an additional energetic stabilization of the wurtzite structure.

III.C.2. X-ray Photoelectron Spectroscopy (XPS). We have acquired XPS spectra of CuI modified graphite surfaces primarily to check for the presence of contaminating iodide or

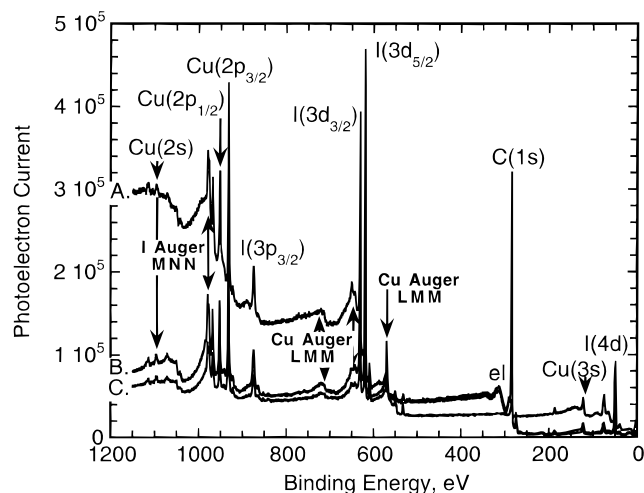


Figure 5. X-ray photoelectron spectra for samples of CuI NCs prepared by the E/C method and a CuI standard: (A) CuI powder (Aldrich, 99.9999%) dispersed on graphite; (B) E/C CuI sample on graphite prepared with an initial copper coverage of $60 \mu\text{C cm}^{-2}$ (or 0.10 equiv copper monolayers); and (C) E/C sample prepared with $480 \mu\text{C cm}^{-2}$ (or 0.85 equiv monolayers) of Cu^0 . The assignment of prominent photoelectron peaks is indicated.

potassium salts. Shown in Figure 5 are X-ray photoemission survey spectra for graphite electrode surfaces on which copper nanocrystallites were first deposited at two coverages: $60 \mu\text{C cm}^{-2}$ (or 0.10 equiv copper monolayers³³) and $480 \mu\text{C cm}^{-2}$ (or 0.85 equiv monolayers). The copper nanocrystallites on these surfaces were then oxidized and exposed to I^- as described above. For purposes of comparison, an XPS spectrum of a 99.9999% γ -CuI standard (also dispersed on HOPG) is also shown. For the two electrodeposited samples, survey spectra revealed no traces of other ions which were present in the copper plating solution or the KI solution (principally nitrate, potassium, and sulfate). In fact, all of the peaks present in these two spectra are assignable to copper, carbon, iodine, or oxygen (not labeled) and are in excellent qualitative agreement with the CuI standard. From a quantitative standpoint, the Cu $2p_{3/2}$ photoemission peak for both electrodeposited samples at 932.3 eV matches that of the standard and is in good agreement with the value of 932.4 eV reported for Cu(I) species such as Cu_2O and CuCl .³⁴ However, because Cu^0 and Cu^{2+} photoemission lines are close to that for Cu^+ , the presence of these other species on the surface cannot be excluded by the XPS data.

II.C.3. Noncontact Atomic Force Microscopy (NC-AFM).

Previously we have shown that NC-AFM allows silver nanocrystallites prepared by pulsed potentiostatic deposition on graphite surfaces to be sized, and the spatial distribution of these particles on the surface to be determined.¹⁴ STM and conventional repulsive mode AFM are not useful for this purpose because interactions of the STM or AFM tip with weakly physisorbed silver particles cause the displacement of these particles on the surface during imaging. For the CuI particles prepared using the E/C method, we have again employed NC-AFM to measure particle heights and height distributions.

Two types of CuI deposits were obtained using the E/C procedure depending on the quantity of copper deposited in the first step of the synthesis: For low copper loadings in the range $40 \mu\text{C cm}^{-2} < Q_{\text{Cu}} < 100 \mu\text{C cm}^{-2}$ (henceforth the “low-coverage regime”, corresponding to 0.07–0.18 equiv copper monolayers assuming an adsorption electrovalency of 2.0), CuI

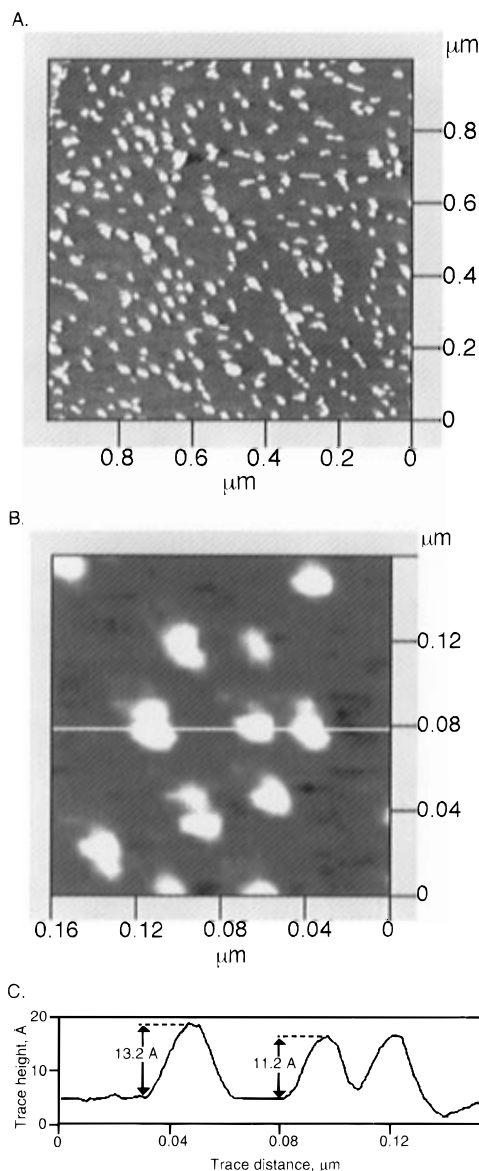


Figure 6. (A) Noncontact atomic force microscopy (NC-AFM) image of CuI nanocrystallites prepared using the E/C method on graphite. The initial copper coverage on this surface was $Q_{\text{Cu}} = 47 \mu\text{C cm}^{-2}$, corresponding to 0.083 equiv copper monolayers. (B) NC-AFM image of a small cluster of CuI NCs. (C) Amplitude trace corresponding to the white line in panel B, highlighting the asymmetry in the particle height as compared with the apparent diameter. This asymmetry is characteristic of the noncontact imaging mode, as described in the text.

NCs were obtained with mean heights ranging from 13.4 to 24.1 Å, and these NCs were well-separated from each other on the graphite surface. *It is this low-coverage regime on which we focus attention in this paper.* At significantly higher initial copper loadings (henceforth the “high-coverage regime”), a more heterogeneous surface was obtained on which discrete CuI NC growth was often combined with the growth of a CuI layer. CuI NCs as large as 200 Å were observed in this regime.

Typical NC-AFM images of three sample surfaces are shown in Figures 6–8. In Figure 6A is shown a $\approx 1.0 \mu\text{m}^2$ region of a surface following an E/C synthesis involving an initial Coulombic loading for copper of $Q_{\text{Cu}} = 47 \mu\text{C cm}^{-2}$, representative of NC-AFM images for CuI NCs prepared in the low-coverage regime. As is apparent from this image, CuI NCs are well-separated from one another on the atomically smooth graphite basal plane surface. The cross section shown in Figure 6C indicates that the apparent diameter of the electrochemically deposited copper particles (200–400 Å) was larger by a factor

(33) The deposition of a closest packed monolayer of copper is predicted to require 564 mC cm^{-2} assuming a nearest neighbor distance of 2.56 Å and an electrosorption valency of 2.

(34) Gaarenstroom, S. W.; Winograd, N. *J. Chem. Phys.* **1977**, *67*, 3500.

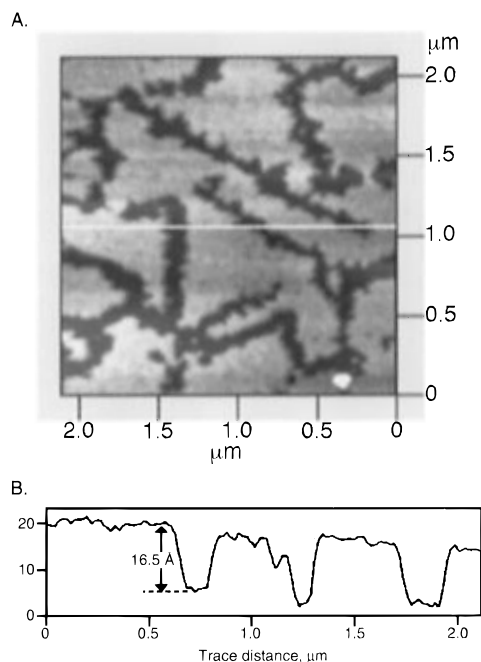


Figure 7. (A) NC-AFM image of CuI layer on a surface which was prepared with an initial copper coverage of $Q_{\text{Cu}} = 290 \mu\text{C cm}^{-2}$ corresponding to ~ 0.5 equiv copper monolayers. (B) Amplitude trace corresponding to the white line indicated in the image of panel A.

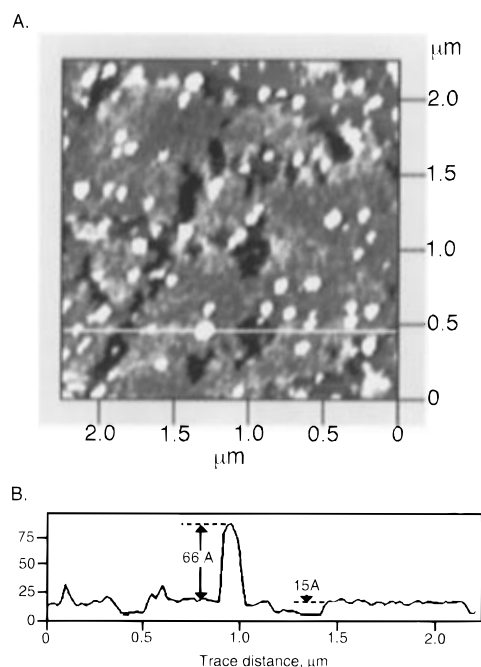


Figure 8. (A) NC-AFM image of CuI layer on a surface which was prepared with an initial copper coverage of $Q_{\text{Cu}} = 453 \mu\text{C cm}^{-2}$ corresponding to ~ 0.8 equiv copper monolayers. (B) Amplitude trace corresponding to the white line indicated in the image of panel A.

of $\approx 20\text{--}40$ compared with the height of $\approx 11\text{--}14$ Å. This diameter–height asymmetry was observed for CuI and copper oxide particles in all the NC-AFM experiments conducted in connection with this paper, and in previous work involving silver NCs.^{14,15} It is now well-appreciated that the *apparent* diameter of protrusions which are rendered with an AFM contains a contribution from the geometry of the AFM probe tip. Because long-range interactions are important in the NC-AFM experiment, the nature of the tip convolution is more complicated than for repulsive mode AFM, and the intrinsic in-plane resolution of the technique is clearly lower. Height measurements of

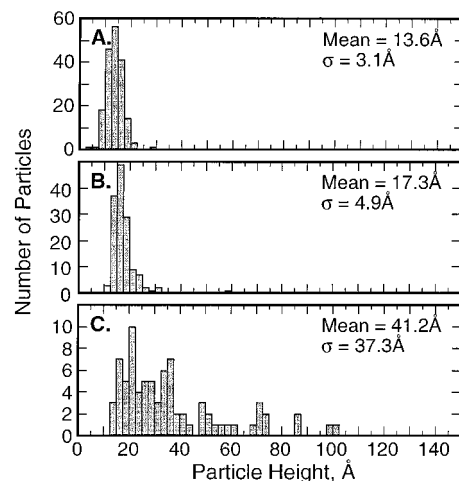


Figure 9. Histograms of CuI particle heights measured from NC-AFM image data for three samples as described in the text.

nanostructures, in contrast, are comparatively accurate since this measurement is insensitive to the precise AFM probe tip geometry.

The statistical analysis of several such regions yielded a mean particle height of 13.4 ± 2.9 Å for this sample and a particle height distribution which is plotted in the histogram of Figure 9A. Statistical data for another sample having a mean particle height of 17.8 ± 4.9 Å are plotted in Figure 9B. The relative standard deviations (RSD) of 22% and 28% seen for these two samples were typical of the CuI NCs populations obtained using the low-coverage regime specified above. The mean CuI particle diameter observed for such syntheses varied from 13.4 to 24.1 Å, but this size did not correlate well with the Coulombic loading because the particle areal density varied substantially from 5×10^9 to $5 \times 10^{10} \text{ cm}^{-2}$.

In the high-coverage regime, the polydispersity of the CuI NC height substantially increased, and the growth of a CuI layer on some regions of the sample surface was also frequently observed. For copper coverages in the range $100 < Q_{\text{Cu}} < 350 \mu\text{C cm}^{-2}$, for example, this copper layer was typically 14–18 Å in thickness. An NC-AFM image of such a layer, for a surface on which both CuI particles (mean height = 17.8 Å) and the CuI layer were present in different regions, is shown in Figure 7A. The linear troughs which traversed these layers were oriented at 60° angles with respect to one another, reflecting the periodicity of the underlying graphite substrate surface. The histogram of Figure 9C documents the distribution of particle sizes for this sample. At yet higher copper coverages of $Q_{\text{Cu}} > 350 \mu\text{C cm}^{-2}$, the growth of large CuI NCs was often observed atop this ≈ 16 Å thick CuI layer, and at defects as well as directly atop the graphite substrate surface. A typical NC-AFM image is shown for a sample prepared using $Q_{\text{Cu}} = 452.7 \mu\text{C cm}^{-2}$ in the NC-AFM image of Figure 8A. These larger CuI NCs were quite nonuniform in diameter, typically ranging from 18 Å to more than 80 Å in height. The origin of the pronounced discontinuity between the epitaxial growth of CuI NCs which is seen in the low-coverage regime and the far more heterogeneous CuI nanoparticle and layer growth seen in the high-coverage regime is incompletely understood at present.

II.C.4. Fluorescence Spectroscopy. Fluorescence spectra were obtained for the graphite-supported CuI NCs prepared using the E/C method. All spectra were acquired at room temperature using an excitation energy of 3.53 eV or 351 nm (as described in greater detail in Experimental Methods). The fluorescence emission from a $\approx 30 \mu\text{m}$ diameter region of the graphite surface was sampled in each spectrum.

Fluorescence spectra for three sample surfaces are shown in Figure 10. Mean particle heights, determined using NC-AFM

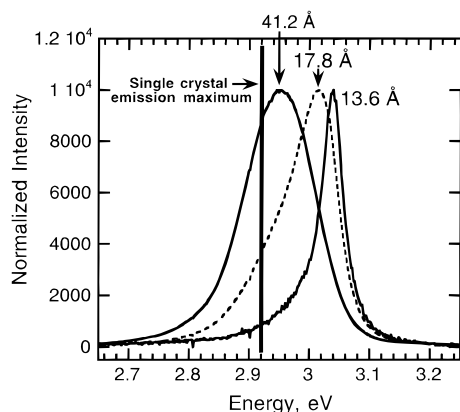


Figure 10. Room temperature fluorescence emission spectra for three CuI NC samples having mean particle sizes, measured from NC-AFM image data, as indicated. These three samples were prepared with initial copper loadings of $95.1 \mu\text{C cm}^{-2}$ (13.6 Å diameter), $587 \mu\text{C cm}^{-2}$ (17.8 Å), and $916 \mu\text{C cm}^{-2}$ (41.2 Å). The peak intensity of each spectrum has been normalized to 10 000 counts.

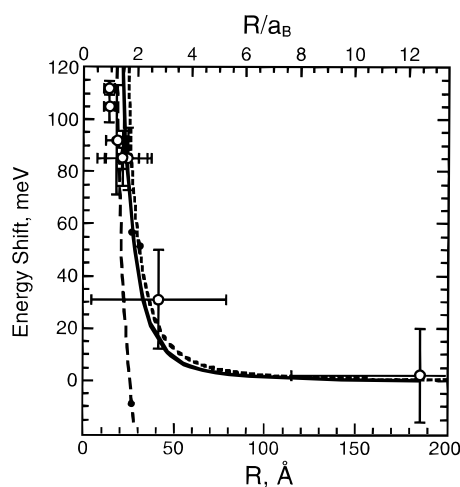


Figure 11. Plot of the shift of the fluorescence emission maximum, measured from 2.92 eV, as a function of the particle height. Vertical and horizontal error bars in this figure represent ± 1.0 standard deviation for the emission maximum (which was sampled at ~ 20 different 30 nm diameter spots), and the particle height (which was sampled at ~ 10 separate $1 \times 1 \mu\text{m}$ regions of the electrode surface). These regions represented the entire ~ 8 mm diameter of the electrode. Solid or broken lines represent the behavior expected on the basis of three theoretical models as follow: The solid line represents the prediction of the variational calculation of Kayanuma (ref 19) for CuI with no adjustable parameters (as described in the text); the short-dashed line is the prediction of eq 1 (weak or exciton confinement); and the long-dashed line is the prediction of eq 2 (strong confinement).

measurements, were 13.6 ± 3.1 Å, 17.8 ± 5.9 Å, and 41.2 ± 37.3 Å for these three samples. Two significant effects of the particle size on the emission characteristics of these CuI NCs are apparent from these spectra: First, the energy of maximum emission is shifted higher with decreasing particle diameter. For the 13.6 Å NCs, a blue shift of ≈ 120 meV is seen versus the emission maximum of 2.92 eV measured for large ($> 1.0 \mu\text{m}$) CuI crystallites. Second, the emission line width is narrowed appreciably for smaller CuI NCs: The full width at half-maximum (fwhm) of the emission for the sample having a 13.6 Å mean was 45.9 meV as compared with 139 meV for the 41.2 Å sample.

The wavelength of maximum emission is plotted in Figure 11 as a function of the CuI NC height for the three samples of Figure 10, plus six additional samples. The horizontal error bars denote 2σ for the NC-AFM-measured particle heights, and

vertical error bars were calculated by taking 2σ for the emission maximum measured at ≈ 20 different 30 μm diameter regions of each sample surface. Seven of these samples, all having particle heights of less than 25 Å, were prepared using an initial copper coverage in the low-coverage regime and therefore represent surfaces on which CuI NCs are epitaxially aligned and well separated laterally on the surface (as confirmed using the NC-AFM measurements). The two samples with mean diameters at 41.2 and 180 Å were high copper coverage samples and exhibited large spatial variations of both the particle height and, as qualitatively expected, the emission maximum of the fluorescence emission.

The energy associated with fluorescence emission from semiconductors is usually somewhat lower than the energy of the band gap (as measured using absorption spectroscopy) because the transition responsible for emission involves trap states located at energies below the conduction band edge. The published luminescence spectra for CuI nanocrystals of Itoh et al.²⁰ and Masumoto et al.¹⁷ both show evidence for carrier trapping; however, the energy of the trap state has depended on such synthesis parameters as the annealing temperature. Absorption spectra for CuI nanocrystals prepared using the E/C method have not yet been obtained, and the existence of carrier trapping cannot, therefore, be detected. However, the particle size dependence of the emission energy can be compared with theoretical models which predict the dependence of the band gap on particle size. Data for three such models are included in the plot of Figure 11: The solid line represents the energy shift predicted using the variational calculation of Kayanuma¹⁹ for spherical semiconductor particles, and the dashed lines (described in greater detail below) are plots of two analytical equations which describe the behavior in the strong and weak confinement limits. With respect to the variational calculation, adapting the results of this theory to CuI involves no adjustable parameters, and the agreement with the experimental data seen in Figure 11 is quite good. For the smallest particles investigated in this study, however, the calculated shift is greater than that which was observed experimentally. In fact, qualitatively similar discrepancies have been seen for comparisons of experimental data for CuCl^{36,37} and CdS³⁶ NCs with this theory. Kayanuma has subsequently shown³⁸ that this discrepancy is largely due to “incomplete confinement” of the electron and hole at the surface of the NC; that is, an invalid assumption of his original variational calculation¹⁹ is that the tunneling of these particles into the medium surrounding the NC is neglected.³⁸ A conclusion of this comparison with theory is that for E/C synthesized CuI nanocrystals, the trap state involved in emission is located close to the conduction band edge in energy. This conclusion is necessarily tentative, however, because bulk values of the dielectric constant and the carrier masses were employed in the calculation of the shift for the theory of Kayanuma.

The dashed lines represent calculations corresponding to two limiting cases for the quantum size effect which are normally distinguished: A *weak (or exciton) confinement* regime exists in the limit $R/a_B \gg 1$ (where R is the NC radius and a_B is the Bohr exciton radius). In this limit, the translational motion of correlated electron–hole pairs (or excitons) is confined, but the extra energy associated with creating an exciton in the NC is small. For weak confinement, Kayanuma¹⁹ has again shown that the relationship between the energy of the first excited state,

(35) Electron and hole effective masses, however, have not been measured for β -CuI, and values of $m_e = 0.33m_0$ and $m_h = 1.4m_0$ for γ -CuI, taken from ref 40, were therefore employed instead. The high-frequency dielectric constant for CuI was taken to be $\epsilon^* = 4.58$ (ref 42).

(36) Ekimov, A. I.; Efros, A. L.; Onushchenko, A. A. *Solid State Commun.* **1985**, *56*, 921.

(37) Itoh, T.; Kirihara, K. *J. Lumin.* **1984**, *31/32*, 120.

(38) Kayanuma, Y.; Momiji, H. *Phys. Rev. B* **1990**, *41*, 10261.

E , and the NC radius, R , may be approximated¹⁹ as

$$E \cong E_g + \frac{\hbar^2}{2M} \frac{\pi^2}{[R - 1.28a_B]^2} \quad (1)$$

where E_g is the band gap in the limit of large R , and M is the exciton mass.³⁹ Equation 1 is plotted as the short-dashed line in Figure 11. In the *strong confinement* limit, in contrast, $R/a_B \ll 1$, and electrons and holes are confined as discrete entities. The energy of the first excited state for this case is given (originally by Brus¹⁸) as

$$E \cong E_g + \frac{\hbar^2 \pi^2}{2R^2} \left[\frac{1}{m_e} + \frac{1}{m_h} \right] - \frac{1.786e^2}{\epsilon R} \quad (2)$$

where m_e and m_h are the effective masses of the electron and hole.³⁵ Equation 2 is plotted as the long-dashed line in Figure 11. The kinetic energies of the electron and hole, given by the second term of eq 2, increase in proportion to $1/R^2$. This kinetic term is partially offset by the Coulomb attraction between the electron and hole which increases in proportion to $1/R$.¹⁸ The relative magnitude of this Coulomb correction is much greater than that which is generally applied in investigations of II–VI materials such as CdSe because of the much larger hole effective mass for CuI (e.g., $m_p = 1.4m_0$ (CuI)⁴⁰ versus 0.45 (CdSe)⁴¹), combined with the smaller dielectric constant of this material (e.g., $\epsilon_\infty/\epsilon_0 = 4.58$ (CuI)⁴² versus 10 (CdSe)⁴¹). This term has been omitted from the strong confinement equations employed in one previous study of the quantum size effect for CuI NCs.¹⁷

The applicability of eqs 1 and 2 to experimental systems was the subject of a theoretical investigation by Kayanuma¹⁹ in which it was concluded that agreement with eq 1 should be observed for $R/a_b \geq 4$ whereas eq 2 is applicable for $R/a \leq 2$. An intermediate size regime, $2 \leq R/a_b \leq 4$, therefore exists where the particle-size dependence of the energy is adequately described by neither equation. On the basis of these criteria, CuI NCs (having an exciton radius, $a_b = 15 \text{ \AA}$) should exhibit strong confinement for $R < 30 \text{ \AA}$ and weak confinement for $R > 60 \text{ \AA}$. Our experimental data do not provide a detailed probe of the size regime in which weak confinement is expected for CuI; however, seven samples were prepared for which $R < 25 \text{ \AA}$, and the emission data for these surfaces are seen in Figure 11 to be in excellent agreement with the predictions of the strong confinement model. The weak confinement model also comes surprisingly close to the variational calculation and eq 2 in this radius regime despite the fact that Kayanuma has shown eq 1 to be invalid for particles in this radius regime. The fortuitous agreement seen for eqs 1 and 2 in Figure 11 (and previously^{20,21}) may account for the misassignment of the quantum size effect for CuI NCs as “weak”. Once again, however, it is important to note that bulk values of the dielectric constant and the carrier masses were employed for all three of the theoretical models, and the quality of the fit must therefore be considered to be somewhat fortuitous.

The emission line width is plotted versus R in Figure 12 for all of the samples investigated in this study. A smooth decrease in line width is seen from 140 meV (for $R = 180 \text{ \AA}$) to less than 50 meV (for $R = 13.6 \text{ \AA}$). For the smallest NCs prepared, the line widths we have observed are considerably narrower than any seen for CuI NCs previously, even for fluorescence

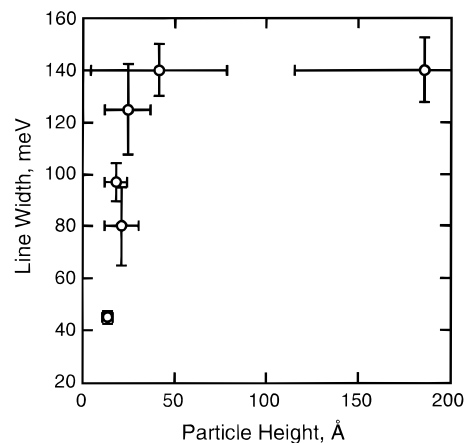


Figure 12. Fluorescence peak width (fwhm) versus particle size for six CuI NC samples. Vertical and horizontal error bars were obtained using the same procedure as in Figure 11.

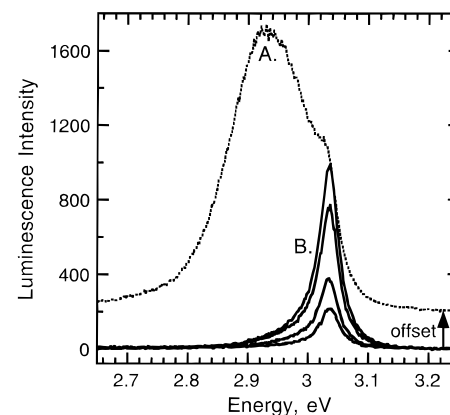


Figure 13. Fluorescence emission spectra for various $30 \mu\text{m}$ diameter regions of a surface having a mean CuI NC height of 15 \AA . The dashed spectrum is for a single microcrystallite, at a step edge on the surface, which was visible by dark-field optical microscopy of the surface. Solid spectra were obtained at four other regions of the same surface where, however, no light-scattering signals could be observed (indicating the existence of no microcrystallites).

spectra acquired at 2 K.⁴³ Our CuI NC samples also exhibit an extremely narrow dispersion of the emission maximum across the sample surface, and together these two indicators are consistent with the narrow NC size distributions plotted in the histograms of Figure 9.

For the larger CuI NCs we have prepared, however, it is useful to ask whether the inhomogeneous broadening which is observed is caused by *particle size dispersion* on the sample surface (which clearly exists), or whether broad fluorescence is an intrinsic property of *individual*, large (i.e., $\approx 100 \text{ \AA}$ diameter) CuI NCs. The emission spectra of Figure 13 speak to this issue. Shown in Figure 13 are an emission spectrum for a single CuI microcrystallite (diameter $\approx 1.0 \mu\text{m}$, as determined from dark-field optical microscopy of the surface) and six spectra for different $30 \mu\text{m}$ diameter regions of the surface on which no microcrystallites were present (also as verified using dark-field microscopy). The line width seen for the CuI microcrystallite (dashed line) of 183 meV is much larger than the ≈ 40 meV of the NC spectra (solid lines). Because a single CuI microcrystallite is sampled in this experiment, the implication is that the line width seen for dispersions of larger nanocrystallites in the data of Figure 13 may not derive purely from the size heterogeneity of the surface.

(39) The exciton mass for β -CuI has been estimated previously by Gongolin et al. to be $3.7 m_0$.

(40) Yu, C. I.; Goto, T.; Ueta, M. *J. Phys. Soc. Jpn.* **1973**, *34*, 693.

(41) Sze, S. M. *The Physics of Semiconductor Devices*, 2nd ed.; John Wiley & Sons: New York, 1981.

(42) Ageev, L. A.; Miloslavskii, V. K.; Maksimenko, T. I. *Opt. Spectrosc. (USSR)* **1974**, *36*, 76.

(43) Masumoto, Y.; Wamura, T.; Iwaki, A. *Appl. Phys. Lett.* **1989**, *55*, 2535.

IV. Summary

A hybrid electrochemical/chemical method for synthesizing CuI NCs on electrode surfaces has been described in which copper nanocrystallites, prepared by a potentiostatic pulse method, are first electrochemically oxidized to Cu₂O and then exposed to an aqueous KI solution in which the oxygen is displaced by iodide to yield β -CuI NCs. The smallest β -CuI NCs prepared using this method, having radii in the range 13–25 Å, are narrowly dispersed in size and are epitaxially aligned with the graphite substrate surface. These NCs exhibit a room temperature fluorescence envelope which is strongly blue-shifted in accordance with the expectations of the calculations of Kayanuma and the strong confinement model of Brus.

Relative to existing experimental methods for preparing size-monodisperse semiconductor NCs, the advantages of the E/C method are the following: (1) *No functionalization of the nanocrystallite surface* is required to prevent aggregation (because incipient semiconductor particles remain anchored to the graphite surface during the conversion from metal to oxide to iodide). (2) The epitaxial alignment seen by SAED indicates that β -CuI NCs interact strongly with the graphite surface and imply that these particles are in *electrical contact* with the graphite electrode surface. (3) *Extremely small semiconductor NCs may be prepared using the E/C method.* The 13.6 Å radius CuI NCs investigated in this study, for example, contained fewer than 10 primitive CuI unit cells. (4) The E/C method is *inexpensive and fast*: The synthesis of β -CuI NC samples required less than 30 min. (5) In principle, the E/C method has *excellent versatility* for the preparation of a variety of semiconductor metal salts. Straightforward extensions of the procedure described here for CuI synthesis should permit the preparation of NCs of other group I–VII and II–VI compounds, as well as NCs of semiconducting metal oxides. (6) The E/C method works well on the graphite basal plane. This is advantageous for two reasons: First, highly oriented pyrolytic graphite can be made thin enough (<400 Å) for SAED characterization of products and intermediates. Second, relative

to most transition metals, graphite has an extremely low density of states ($2.5 \times 10^{20} \text{ cm}^{-3}$)⁴⁴ and, perhaps for this reason, does not efficiently quench the fluorescence of the semiconductor NCs disposed on its surface. For both of these reasons, future fundamental investigations of nanometer-scale materials synthesized using the E/C method will be facilitated by performing the E/C synthesis on graphite.

A disadvantage of the E/C method in the case of CuI is that the monodispersity of large (i.e., diameter > 25 Å) CuI NCs is poor because the well-defined Volmer–Weber deposition mode is lost for copper as NCs attain a height of ≈ 25 Å. We have recently reported a similar effect for the growth of silver NCs in which silver deposition abruptly becomes disordered at a NC height of 40 Å.¹⁴ In order to further extend the applicability of the E/C method, the origins of polydispersity in metal NCs growing under diffusion control must be better understood. Additionally, a more detailed, atomic-scale understanding of the conversion from Cu⁰ to Cu₂O to CuI is needed and must await further investigations of these processes.

Acknowledgment. The authors express their appreciation to Mr. Art Moore of Advanced Ceramics for donations of highly oriented pyrolytic graphite, to Prof. John Hemminger and graduate student Mickey Laux for performing the XPS measurements, and to Prof. Hemminger for helpful discussions. This work was supported by the Office of Naval Research (N00014-93-1-0757) and the NSF Young Investigator's Program (DMR-9257000). In addition, the following are gratefully acknowledged: two Department of Education GAANN fellowships (G.S.H. and M.G.A.), a Welch Scholarship of the International Union for Vacuum Science (S.G.), and an A. P. Sloan Fellowship, an Arnold and Mabel Beckman Young Investigator award, and a Camille Dreyfus Teacher-Scholar award (R.M.P.).

JA9630755

(44) Gerischer, H.; McIntyre, R.; Scherson, D.; Storch, W. *J. Phys. Chem.* **1987**, *91*, 1930.